https://doi.org/10.5194/egusphere-2025-2298
Preprint. Discussion started: 11 August 2025

From typhoon rainfall to slope failure: optimizing susceptibility models and dynamic thresholds for landslide warnings in Zixing City, China

Weifeng Xiao[1,2], Guangchong Yao[1], Zhenghui Xiao[1], Luguang Luo[1], Yunjiang Cao[1], Wei Yin*[2,3]

[1]School of Earth Sciences and Spatial Information Engineering, Hunan University of Science and Technology, Xiangtan 411201, China
[2]Hunan Geological Disaster Monitoring Early Warning and Emergency Rescue Engineering Technology Research Center, Changsha 410004, China
[3]Hunan Institute of Geological Disaster Investigation and Monitoring, Changsha 410004, China

Corresponding author.
E-mail address: 379118944@qq.com (Wei Yin)

Abstract: From typhoon rainfall to slope failure, this study addresses the urgent need for typhoon-adapted hazard warning systems in mountainous regions like Zixing City, China. We develop an integrated framework to optimize dynamic susceptibility models and rainfall thresholds by leveraging machine learning and spatiotemporal rainfall analysis. Using buffer-based negative sampling (0.1–5.0 km) and variable weighting methods (IV, CF, FR), we compare SVM and LightGBM models. The SVM model with FR input at 0.5 km buffer achieved the highest accuracy (AUC=0.913), correctly classifying 86.4% of landslides in high-risk zones, revealing how typhoon-driven hydrology interacts with slope instability. For rainfall thresholds, the H24-D7 model (24-hour intensity vs. 7-day antecedent rainfall) emerged as optimal (71.8% accuracy), effectively capturing typhoon-specific triggers like short-term downpours and cumulative soil saturation. Kriging interpolation generated spatially explicit thresholds, identifying granite slopes and road-proximal areas as hotspots for typhoon-induced failures. The final hazard warning system, integrating susceptibility and dynamic thresholds, showed 71.4% overlap with historical landslides, emphasizing the critical role of typhoon rainfall dynamics in slope failure prediction. This work provides a scalable approach for regions facing typhoon-related landslide risks, prioritizing both spatial heterogeneity and temporal rainfall patterns.

Keywords: Typhoon-induced landslide; Slope failure; Hazard warning system; Dynamic thresholds; Landslide susceptibility mapping

1 Introduction

Landslides are among the most devastating natural hazards, particularly in regions with steep terrain, complex geology, and high rainfall variability (Thiene et al., 2017; Froude and Petley, 2018). As rapid urbanization and climate change exacerbate the frequency of typhoon-induced extreme precipitation events in coastal and mountainous regions like Zixing City, landslide risks have escalated, threatening lives and infrastructure (Gariano and Guzzetti, 2016; Fan et al., 2018). Typhoons, characterized by prolonged antecedent rainfall and short-duration high-intensity bursts, uniquely drive slope failures through cumulative soil saturation and abrupt hydrological stress (Yang et al., 2017). This situation underscores the urgent need for advanced hazard prediction systems capable of addressing region-specific triggers such as typhoon rainfall patterns (Segoni et al., 2018a; Regmi et al., 2024). Despite progress in landslide susceptibility prediction (LSP) and rainfall threshold modeling, critical challenges remain. These challenges include addressing data imbalances, optimizing variable selection, and refining the integration of spatiotemporal risk assessments under dynamic meteorological conditions.

A major challenge in LSP arises from the imbalance between landslide (positive) and non-landslide (negative) samples (Pourghasemi and Rahmati, 2018; Lv et al., 2022; Sun et al., 2023). The relatively sparse distribution of landslides compared to stable areas leads to datasets dominated by negative samples, complicating model training (Lombardo and Mai, 2018). Traditional methods often mitigate this imbalance by randomly sampling non-landslide points across the study area (Steger et al., 2016; Dou et al., 2023). However, such random selection may introduce spatial bias, as non-landslide points may still include areas prone to instability that are not yet identified (Kalantar et al., 2018).

To overcome this limitation, recent approaches have employed buffer-based negative sampling, systematically excluding non-landslide points near known landslides (Reichenbach et al., 2018; Chen et al., 2017b; Yan et al., 2023). This method assumes that adjacent areas share similar environmental conditions (e.g., slope, lithology) and should not be classified as "stable" (Achu et al., 2022; Huang et al., 2020). Various buffer distances have been tested, ranging from tens to thousands of meters, with the optimal buffer distance being region-specific (Yan et al., 2019; Chen et al., 2017a). However, the influence of buffer distance, variable selection methods (e.g., information value (IV), certainty factor (CF), frequency ratio (FR)), and machine learning model architecture on predictive performance remains underexplored, limiting the generalizability of current frameworks.

Landslide susceptibility prediction aims to identify areas prone to slope failure based on static environmental factors such as topography, lithology, land cover, and hydrology (Zêzere et al., 2017; Guo et al., 2024). Traditional methods often use deterministic and statistical approaches, including frequency ratio (FR), logistic regression (LR), and weight of evidence (WOE), which quantify the correlation between historical landslides and predisposing factors through linear or semi-linear relationships (Ciurleo et al., 2017; Reichenbach et al., 2018). However, these methods typically oversimplify the complex, nonlinear interactions that govern slope stability (Merghadi et al., 2020).

Machine learning (ML) algorithms, such as support vector machine (SVM) and light gradient boosting machine (LightGBM), have emerged as powerful alternatives. SVM excels in high-dimensional classification, identifying optimal hyperplanes to differentiate between landslide-prone and stable areas, even in imbalanced datasets (San, 2014; Huang and Zhao,

https://doi.org/10.5194/egusphere-2025-2298
Preprint. Discussion started: 11 August 2025

2018). LightGBM, a gradient-boosted decision tree method, enhances scalability and computational efficiency, making it well-suited for large, complex geospatial datasets (Sun et al., 2023). Both models offer superior predictive accuracy by capturing intricate relationships among variables without restrictive assumptions (Yang et al., 2023; Zhang et al., 2022). However, the performance of ML models is sensitive to the choice of input variables and sampling strategies, and a comparative analysis of commonly used variable weighting methods (e.g., IV, CF, FR) in combination with ML algorithms remains limited.

In addition to spatial susceptibility, temporal landslide prediction requires the definition of rainfall thresholds—cumulative or intensity-duration (I-D) rainfall values that trigger slope failure. For typhoon-prone regions like Zixing City, dynamic thresholds must account for both short-term extreme rainfall bursts and prolonged antecedent precipitation patterns (Guzzetti et al., 2020; Guzzetti, 2021). Traditional empirical methods for deriving regional rainfall thresholds often fail to address local geological and environmental variability, leading to generalized thresholds that reduce prediction accuracy (Segoni et al., 2018a; Piciullo et al., 2018). Recent approaches integrate multi-temporal rainfall parameters and advanced statistical techniques to optimize thresholds for diverse triggering mechanisms.

Spatial interpolation methods, such as Kriging, have also been applied to generate continuous rainfall threshold surfaces, allowing for local variations in geological and environmental conditions (Huang et al., 2022; Segoni et al., 2018b). When combined with high-resolution susceptibility maps, this approach supports the development of integrated hazard warning systems that dynamically adapt to typhoon rainfall scenarios (Piciullo et al., 2017; Mirus et al., 2018).

In this study, we focus on Zixing City, located in the mountainous southern region of Hunan Province, China, a region frequently impacted by typhoon-induced extreme rainfall, as a representative case study for the development of an integrated framework for optimizing landslide susceptibility prediction and determining rainfall thresholds. Following the landfall of Typhoon "Gemei" in July 2024, which triggered over 700 landslides, Zixing's unique geo-environmental conditions provide an ideal setting for investigating typhoon-driven landslide mechanisms. The specific objectives of this study are as follows: (1) to identify optimal buffer distances for negative sampling to mitigate spatial bias in imbalanced datasets; (2) to evaluate the effectiveness of variable weighting methods (IV, CF, FR) in combination with machine learning algorithms (SVM, LightGBM) for improving landslide susceptibility prediction accuracy; (3) to optimize dynamic rainfall threshold models for typhoon rainfall, distinguishing between short-term high-intensity bursts (e.g., 24-hour rainfall) and long-term antecedent moisture (e.g., 7-day effective rainfall); (4) to apply Kriging interpolation to generate spatially continuous rainfall threshold surfaces that consider local geological and environmental variability; and (5) to integrate the optimized susceptibility maps with the interpolated rainfall thresholds to develop a comprehensive hazard warning system for typhoon-induced landslides.

2 Study area and data sources

2.1 Study area

Zixing City, situated in southeastern Hunan Province, China (25°34′–26°18′ N, 113°08′–113°44′ E), spans 2,746 km² and is characterized by rugged topography, with over 200 peaks exceeding 800 meters in elevation (Fig. 1). As a typhoon-prone mountainous region in southern Hunan, it faces direct impacts from Pacific typhoons, which impose dual hydrological threats: (1) prolonged pre-typhoon antecedent rainfall that gradually saturates slopes and (2) short-duration extreme rainfall during landfall that induces abrupt hydrological stress. For example, Typhoon 'Gemei' in July 2024 unleashed 412.7 mm of rainfall, triggering over 700 landslides and underscoring the urgent need for typhoon-specific hazard monitoring systems tailored to its geo-environmental conditions.

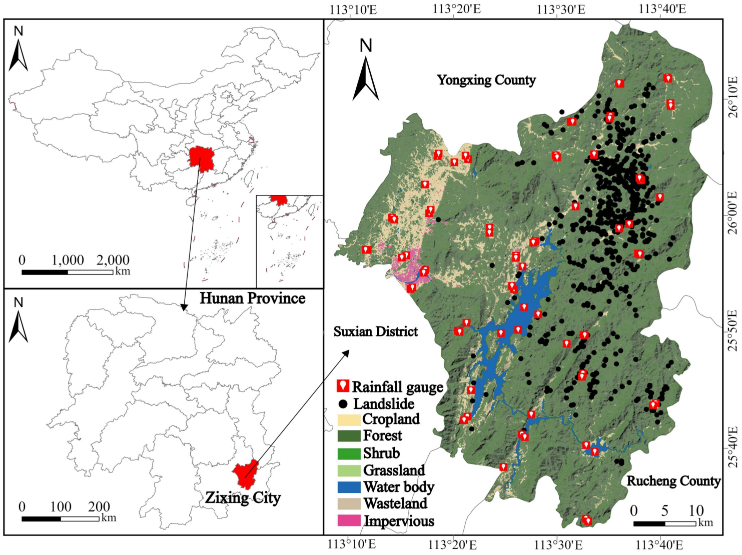

Figure 1. Geographical distribution of the study are, landslides and rainfall gauges.

2.2 Data collection and preprocessing

2.2.1 Compilation of landslide catalogue

Constructing an accurate landslide catalogue is crucial for landslide susceptibility prediction (Reichenbach et al., 2018). In this study, a total of 705 landslide events triggered by Typhoon “Gemei” on July 27, 2024, were documented. The dataset was obtained from the Hunan Center for Natural Resources Affairs, verified through field inspections and satellite imagery to ensure accuracy.

2.2.2 Landslides-related conditioning factors

Identifying key conditioning factors is essential for delineating landslide-prone areas. Based on literature reviews and the study area’s geo-environmental characteristics, twelve factors were selected, including elevation, slope gradient, slope orientation, curvatures, topographic wetness index (TWI), distance to road, river, fault, normalized difference vegetation index (NDVI), stream power index (SPI), and lithology (Fig. 2).

https://doi.org/10.5194/egusphere-2025-2298
Preprint. Discussion started: 11 August 2025

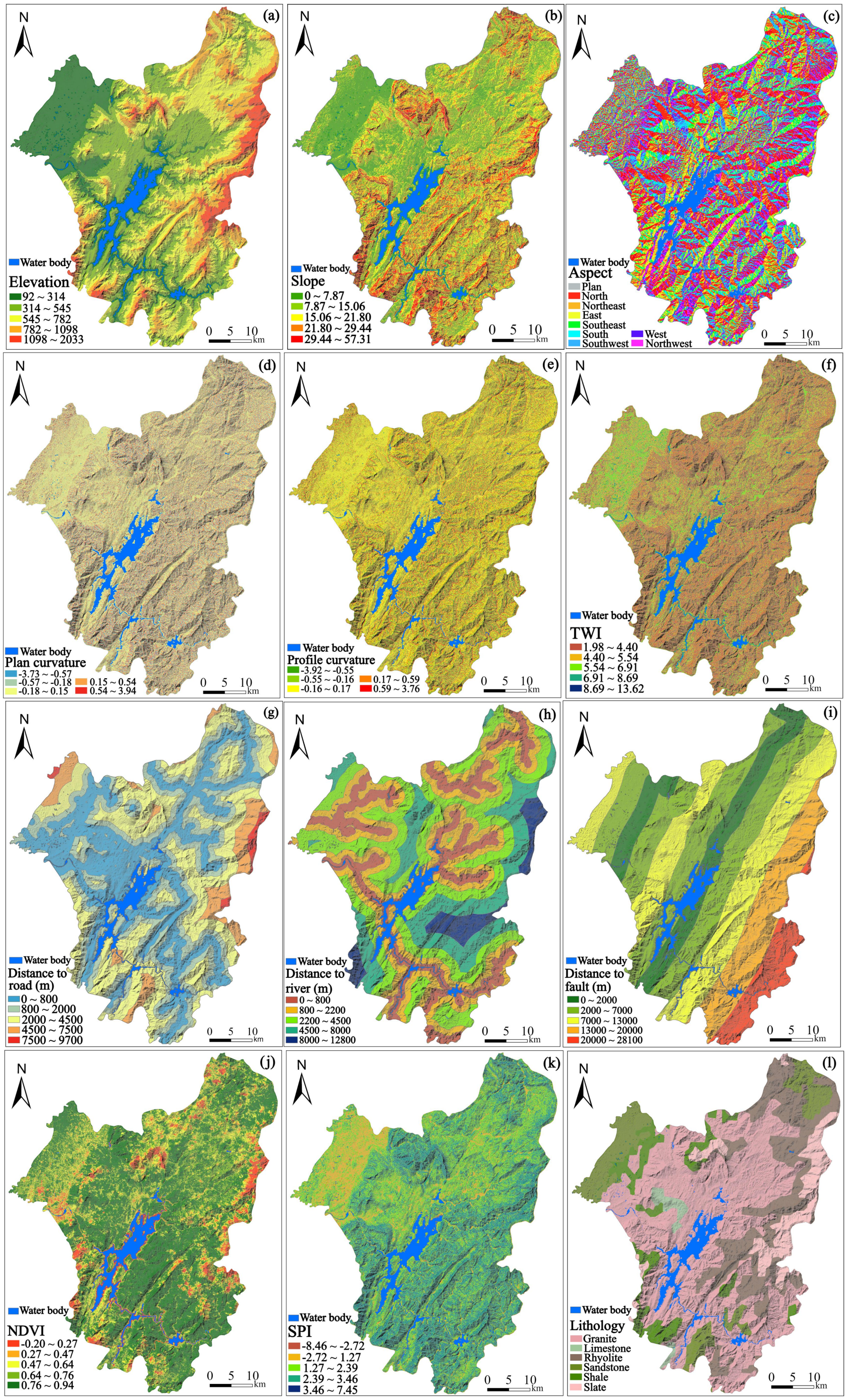

Figure 2. Landslide-related conditioning factors.

Topographic factors, such as elevation, slope gradient, slope orientation, TWI, SPI, and curvature, were extracted from a 30-meter digital elevation model (DEM) sourced from the Geospatial Data Cloud (https://www.gscloud.cn). Environmental factors like NDVI, distances to roads, rivers, and fault lines were derived from 1:50,000-scale cartographic maps and Landsat 8 OLI imagery, both of which were also accessible via the Geospatial Data Cloud. Geological composition and fault line data were obtained from 1:100,000-scale geological maps. Hourly rainfall data from 12 meteorological stations during Typhoon "Gemei" were integrated to support dynamic threshold analysis.

For analysis, the study area was divided into 60 × 60 meter grid cells. Within this grid, 705 landslide events were recorded, each located within a unique grid cell and treated as positive samples for susceptibility analysis.

3 Methodologies

This study proposes an integrated framework for optimizing landslide susceptibility prediction (LSP) and typhoon-specific rainfall thresholds within hazard warning systems (Fig. 3). The framework includes the following key components: (1) landslide susceptibility prediction and mapping, utilizing twelve conditioning factors prioritizing typhoon-induced hydrological responses (e.g., TWI, SPI) and 705 landslide records from July 27, 2024, optimized with five buffer distances and evaluated using ROC curves; (2) dynamic rainfall threshold modeling based on typhoon rainfall parameterization, validated and spatially interpolated using Kriging; and (3) the integration of spatial and temporal probabilities to develop a typhoon-adapted hazard warning system, demonstrated through a case study in Zixing City.

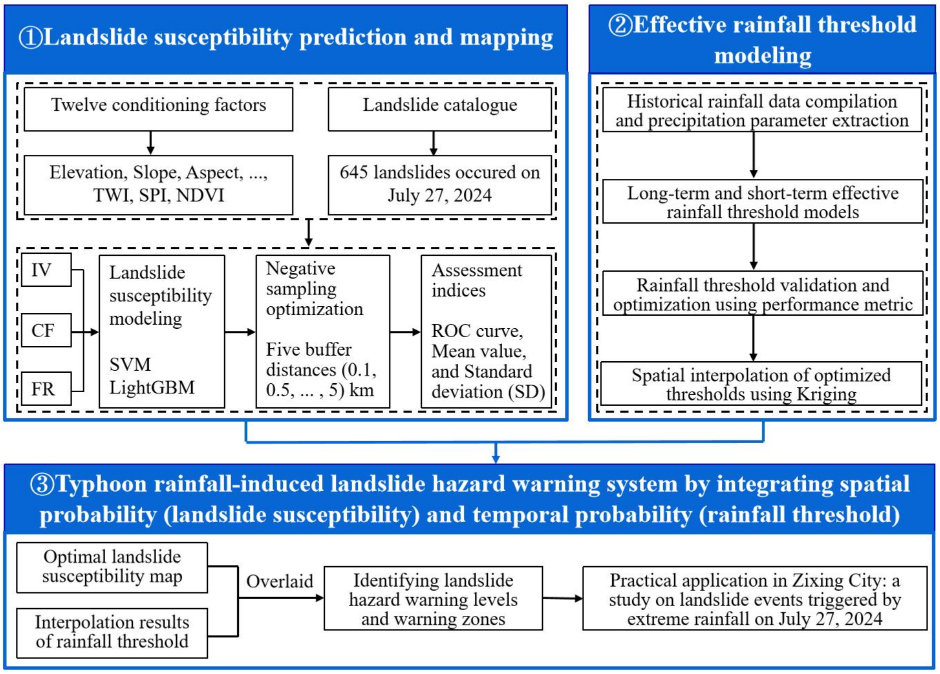

Figure 3. Technical framework for developing a typhoon rainfall-induced landslide hazard warning system.

3.1 Landslide susceptibility prediction and mapping

3.1.1 Machine learning models

SVM is a robust supervised learning algorithm widely used for classification in landslide susceptibility mapping (Kalantar et al., 2018; Wang et al., 2020). It operates by finding the optimal hyperplane that separates landslide-prone areas from stable regions in a multidimensional feature space. For typhoon-triggered landslides, SVM effectively handles imbalanced datasets caused by concentrated slope failures in high-intensity rainfall zones. The SVM optimization problem is defined as:

$$\min_{w,b,\xi} \frac{1}{2} w^T w + C \sum_{i=1}^{n} \xi_i \tag{1}$$

subject to the constraint:

$$y_i (w^T \phi(x_i) + b) \geq 1 - \xi_i, \quad \xi_i \geq 0, \quad i = 1, \cdots, n \tag{2}$$

where w is the normal vector to the hyperplane, b is the bias term, ξ_i are slack variables, C is the regularization parameter, and $\phi(x_i)$ maps input vectors to a higher-dimensional space. The variable y_i represents the class label (-1 or 1) for each sample x_i.

LightGBM is an efficient gradient boosting framework for large datasets, known for training an ensemble of decision trees by iteratively adding trees that minimize errors from previous trees. LightGBM's scalability is critical for processing typhoon-related geospatial data (e.g., hourly rainfall grids) across 2,746 km^2 (Sun et al., 2023; Sahin, 2020). The minimized objective function is expressed as:

$$L = \sum_{i=1}^{N} (y_i - \hat{y}_i)^2 + \lambda \sum_{j=1}^{M} \left\| \theta_j \right\|^2 \tag{3}$$

where y_i is the true label, $\hat{y}_i$ is the predictive value, λ is a regularization parameter, and θ_j represents the parameters of the model.

3.1.2 Input variable weighting methods

The IV method, grounded in information theory, assesses how different factors contribute to landslide susceptibility within a study area (Niu et al., 2024). Factors such as distance to roads and lithology were weighted higher in Zixing City due to their interaction with typhoon-induced soil saturation. The IV for each evaluation factor is determined using the formula below:

$$IV(F_i, K) = \ln \frac{N_i / N}{S_i / S} \tag{4}$$

where $IV(F_i, K)$ is the information value of evaluation factor F_i in relation to landslide event K, N_i refers to the number of landslides, N is the total number of landslides, S_i represents the area covered by factor F_i, and S is the total area of the study area.

The CF is a widely utilized probabilistic technique for assessing the likelihood of landslide events (Zhao et al., 2021). It quantifies the prior probability of a landslide occurring under various influential factor conditions using data from known landslide locations. The expression of CF is as follows:

$$CF = \begin{cases} \dfrac{PP_a - PP_s}{PP_s(1-PP_a)}, & PP_a < PP_s \\ \dfrac{PP_a - PP_s}{PP_a(1-PP_s)}, & PP_a \geq PP_s \end{cases} \quad (5)$$

where *CF* is the certainty factor for potential landslide occurrences, PP_a is the proportion of the number of landslide points relative to the area of the influencing factor's domain, and PP_s is the proportion of the total number of landslide points across the entire study region to the total area of the study region.

The FR is a prevalent method in statistical analysis that assesses the relative impact of various factors on the incidence of landslides (Panchal et al., 2021). An elevated FR value denotes a more significant influence of a factor on the likelihood of landslides. The FR is determined by the following equation:

$$FR = \frac{N_i / N}{S_i / S} \quad (6)$$

where *FR* is the frequency ratio, N_i represents the account of landslides within the area corresponding to the conditioning factor, *N* is the total number of landslides, S_i is the area covered by the conditioning factor and *S* is the total area of the study region.

3.1.3 Buffer distance optimization

Negative (non-landslide) samples are generated by excluding zones within five buffer distances (d=0.1, 0.5, 1.0, 2.0, 5.0 km) around landslide points. For each distance d, negative samples are selected from the remaining stable areas, balanced to match the landslide count (n=705). The optimal buffer is determined by maximizing the receiver operating characteristic curve (AUC) values across distances.

3.1.4 Uncertainty assessment for model performance

To assess the SVM and LightGBM models' performance in predicting landslide susceptibility, we focused on the area under the AUC for both the training and test sets. AUC is a crucial metric for assessing classification models, especially in binary tasks like this. The AUC score quantifies the model's overall ability to distinguish between the positive (landslide) and negative (non-landslide) classes. An AUC value closer to 1 indicates better model performance, reflecting a higher capability to correctly classify instances.

In landslide susceptibility prediction, the mean and standard deviation (SD) are critical metrics indicating central tendency and variability. Generally, a lower mean and SD in LSP distribution suggest lower uncertainty and less spread in predicting landslide susceptibility (Huang et al., 2022).

3.2 Effective rainfall threshold modeling

3.2.1 Rainfall parameterization and threshold calculation

Typhoon-induced landslides are generally influenced by a combination of antecedent moisture conditions and immediate precipitation, rather than by isolated rainfall events (Mondini et al., 2023; Tufano et al., 2021). To account for the cumulative impact of multi-day rainfall while incorporating hydrological processes such as evapotranspiration and drainage, we adopted the concept of effective rainfall (P_e), calculated as:

$$P_e = \sum_{i=0}^{n} k^i P_i \tag{7}$$

where P_i represents the daily rainfall on the i-th day preceding landslide occurrence, n denotes the number of antecedent days considered, and k is the effective rainfall decay coefficient (Segoni et al., 2018a). For hourly rainfall parameterization, P_i is derived as:

$$P_i = \sum_{j=1}^{24} R_{ij} \tag{8}$$

where R_{ij} is the hourly rainfall at the j-th hour of the i-th day.

3.2.2 Long-term and short-term rainfall parameters

Rainfall-triggered landslides are generally triggered by two dominant mechanisms: prolonged low-intensity rainfall and short-duration high-intensity storms. Based on statistical analysis of historical landslide events in Hunan Province (Xiao et al., 2025), a 7-day antecedent period was identified as optimal for characterizing long-term rainfall impacts. Consequently, the 7-day effective rainfall (D7) was selected as the long-term parameter. Short-term rainfall metrics were defined as cumulative precipitation over 1 hour (H1), 12 hours (H12), 24 hours (H24), and 72 hours (H72) preceding landslide initiation. These intervals capture distinct rainfall characteristics: H1 reflects extreme short-term intensity for rapid slope failures, H12 and H24 represent sub-daily to daily precipitation critical for intermediate responses, and H72 accounts for multi-day storm sequences.

3.2.3 Rainfall threshold model development

The threshold modeling framework comprises four sequential steps:

(1) Parameter calculation: For each landslide sample, short-term rainfall parameters (H1, H12, H24, and H72) and the long-term rainfall parameter (D7) are calculated. The ratios of short-term parameters to the long-term parameter are computed as: R1=H1/D7, R12=H12/D7, R24=H24/D7, and R72=H72/D7.

(2) Threshold setting: Long-to-short-term ratio coefficients (RC1, RC12, RC24, and RC72) are introduced as thresholds to determine the dominant rainfall pattern for each landslide. These thresholds are used to classify landslides into short-term or long-term Typhoon-induced categories.

(3) Coefficient optimization: A cyclic trial-and-error method is employed to determine the optimal ratio coefficients (RC1, RC12, RC24, and RC72), maximizing the accuracy and reliability of the model.

3.2.4 Optimal ratio coefficient threshold determination

The process of determining the optimal long-to-short-term ratio coefficient threshold is demonstrated using H12-D7 as an example. The process for the remaining coefficients (H1-D7, H24-D7, and H72-D7) follows a similar approach. A 5-fold cross-validation method is applied, with the following procedure:

(1) Spatial interpolation: Kriging interpolation is applied to short-term and long-term rainfall data from various rain gauge stations within the study area. R12 and D7 values for each landslide are calculated using Equations (7) and (8).

(2) Data preparation: The dataset is divided into five equal parts for cross-validation, with each part serving as a test set while the remaining four serve as the training set.

(3) Initial threshold setting: An initial threshold for RC12 is set based on the minimum value in the training set.

(4) Threshold evaluation: For each fold, the RC12 threshold is compared with the R12 value of samples in the test set. If RC12<R12, the prediction is considered a failure. Prediction accuracy is calculated for each RC12 threshold, adjusting in 0.001 increments until the highest prediction accuracy is achieved.

(5) Optimal RC12 threshold determination: The RC12 threshold with the highest prediction accuracy is selected for each fold. The final RC12 threshold is determined by averaging the optimal thresholds from all five folds.

3.2.5 Spatial distribution of optimal threshold

According to the optimal ratio coefficient threshold determined in section 3.2.4 and the long-term and short-term rainfall parameters obtained through interpolation, the threshold spatial distribution for the study area can be derived. Taking H12/D7 as an example, the process is as follows:

First, by dividing the H12 values of each landslide point by the optimal ratio coefficient RC12, the corresponding D7 thresholds for each landslide point can be calculated. These D7 thresholds serve as a basis for applying the Kriging interpolation method to obtain the spatial distribution map of the D7 thresholds across the entire study area.

Next, by multiplying the D7 values of each landslide point by the ratio coefficient RC12, the corresponding H12 thresholds for each landslide point can be determined. Subsequently, utilizing these H12 thresholds, the Kriging interpolation method is applied once more to generate the spatial distribution map of the H12 thresholds for the entire study area.

3.3 Typhoon-adapted hazard warning system

In order to effectively prevent typhoon-adapted landslide hazards, constructing a comprehensive landslide early warning system is crucial. This system integrates landslide susceptibility prediction with critical rainfall thresholds, combining spatial probability and temporal probability to predict the risk of landslide occurrence and the timing of potential events.

3.3.1 Construction of the hazard warning system

Using the natural breaks point method, the LSP is categorized into five levels of spatial probability: very low (S1), low (S2), moderate (S3), high (S4), and very high (S5). These levels represent varying degrees of susceptibility to landslides in different regions, forming the basis for assessing landslide risks when combined with rainfall data. Paralleling the LSP categorization, rainfall thresholds are also divided into five levels using the natural breaks point method, representing temporal probability: very low (T1), low (T2), moderate (T3), high (T4), and very high (T5). A lower rainfall threshold indicates a higher likelihood of typhoon-induced landslides, thus signaling a greater risk of landslide events.

Table 1. Classification of landslide hazard warning zones by integrating landslide susceptibility levels (S1~S5) with rainfall threshold levels (T1~T5).

Landslide hazard warning zones	T1	T2	T3	T4	T5
S1 (very low)	No warning zone (2nd level)	No warning zone (1st level)	No warning zone (1st level)	No warning zone (1st level)	No warning zone (1st level)
S2 (low)	3rd level warning zone	No warning zone (2nd level)	No warning zone (2nd level)	No warning zone (1st level)	No warning zone (1st level)

S3 (moderate)	4th level warning zone	3rd level warning zone	3rd level warning zone	No warning zone (2nd level)	No warning zone (1st level)
S4 (high)	5th level warning zone	4th level warning zone	3rd level warning zone	No warning zone (2nd level)	No warning zone (1st level)
S5 (very high)	5th level warning zone	5th level warning zone	4th level warning zone	3rd level warning zone	No warning zone (2nd level)

The matrix-based integration of LSP results and rainfall thresholds, as presented in Table 1 (Segoni et al., 2015), highlight the correlation between landslide susceptibility and rainfall intensity. As the levels of landslide hazard warnings escalate from the 1st level, indicating no warning, to the 5th level, which signifies the highest alert, the likelihood of landslide occurrences correspondingly increases. Areas categorized in higher hazard zones correspond to regions with a heightened risk of landslides. This underscores the importance of implementing more effective geological disaster prevention strategies, as thoroughly discussed in the literature by Huang et al. (2022).

4.Landslide susceptibility prediction using machine learning models

4.1 IV, CF and FR values

The IV, CF, and FR values were calculated for various conditioning factors influencing landslide susceptibility. For elevation, the highest FR (1.637) was observed in the 545~782 m range, with a corresponding positive IV (0.389) and CF (0.493). Slope showed a peak FR (1.522) in the 7.87~15.06° range, with higher IV (0.343) and CF (0.420). Aspect revealed that south-facing slopes had the highest FR (1.299), with positive IV (0.230) and CF (0.261). TWI showed the highest FR (1.799) in the range 8.69~13.62, with IV (0.444) and CF (0.587) indicating strong susceptibility. Lithology analysis showed that granite and rhyolite had higher FR values (1.247 and 1.546), while slate and sandstone had much lower FR values, suggesting a greater influence of geological type on landslide occurrence.

Table 2. IV, CF and FR values for each conditioning factor.

Conditioning factors	Factor grading	Landslides	IV	CF	FR
Elevation (m)	92~314	81	-0.493	-0.679	0.507
	314~545	255	0.218	0.246	1.279
	545~782	312	0.389	0.493	1.637

	782~1098	57	-0.505	-0.704	0.495
	1098~2033	0	-1	0	0
Slope (°)	0~7.87	91	-0.347	-0.427	0.653
	7.87~15.06	267	0.343	0.420	1.522
	15.06~21.80	219	0.168	0.184	1.202
	21.80~29.44	112	-0.213	-0.240	0.786
	29.44~57.31	16	-0.756	-1.411	0.2440
Aspect	Plan	0	-1	0	0
	North	74	-0.102	-0.109	0.897
	Northeast	67	-0.058	-0.060	0.942
	East	70	-0.120	-0.128	0.800
	Southeast	105	0.116	0.123	1.131
	South	102	0.230	0.261	1.299
	Southwest	96	0.144	0.156	1.169
	West	96	0.039	0.039	1.040
	Northwest	95	-0.071	-0.074	0.929
Plan curvature	-3.73~-0.57	36	-0.275	-0.321	0.725
	-0.57~-0.18	189	0.250	0.287	1.333
	-0.18~0.15	284	0.000	0.000	1.000
	0.15~0.54	156	-0.059	-0.061	0.941
	0.54~3.94	40	0.373	-0.467	0.627
Profile curvature	-3.92~-0.55	19	-0.608	-0.935	0.392
	-0.55~-0.16	114	-0.240	-0.274	0.760
	-0.16~0.17	260	-0.112	-0.119	0.888
	0.17~0.59	253	0.480	0.392	1.480
	0.59~3.76	59	0.276	0.324	1.382
TWI	1.98~4.40	151	-0.393	-0.499	0.607
	4.40~5.54	297	0.245	0.280	1.324
	5.54~6.91	132	-0.011	-0.011	0.989
	6.91~8.69	73	0.046	0.047	1.048
	8.69~13.62	52	0.444	0.587	1.799
Distance to road (m)	0~800	350	0.333	0.405	1.499
	800~2000	194	-0.011	-0.011	0.989
	2000~4500	153	-0.277	-0.324	0.723
	4500~7500	8	-0.857	-1.942	0.143
	7500~9700	0	-1.000	0.001	0.001
Distance to river (m)	0~800	152	0.147	0.158	1.172
	800~2200	205	0.081	0.085	1.088
	2200~4500	218	0.010	0.010	1.010
	4500~8000	101	-0.229	-0.260	0.771
	8000~12800	29	-0.278	-0.325	0.722
Distance to fault (m)	0~2000	64	-0.380	-0.478	0.620
	2000~7000	262	0.062	0.064	1.066
	7000~12000	286	0.305	0.364	1.439
	12000~18000	62	-0.414	-0.535	0.586
	18000~28100	31	-0.398	-0.508	0.602
NDVI	-0.20~0.27	2	-0.956	-3.133	0.044
	0.27~0.47	29	-0.446	-0.591	0.554
	0.47~0.64	108	0.217	0.245	1.278
	0.64~0.76	296	0.015	0.617	1.854
	0.76~0.94	270	-0.255	-0.295	0.745
SPI	-8.46~-2.72	0	-1.000	0.000	0.000
	-2.72~1.27	108	0.250	0.288	1.334
	1.27~2.39	370	0.229	0.261	1.298

	2.39~3.46	180	-0.320	-0.386	0.680
	3.46~7.45	47	-0.356	-0.440	0.644
Lithology	Slate	8	-0.856	-1.938	0.144
	Shale	10	-0.798	-1.601	0.202
	Limestone	1	-0.907	-2.376	0.093
	Sandstone	3	-0.958	-3.179	0.042
	Granite	485	0.198	0.221	1.247
	Rhyolite	198	0.353	0.436	1.546

4.2 Multicollinearity analysis for landslide-related conditioning factors

To ensure reliable landslide susceptibility evaluations, we addressed the potential issue of multicollinearity among the considered factors using the variance inflation factor (VIF). A VIF score above 10 signifies a strong linear relationship, indicating potential multicollinearity issues.

For both the IV and CF methods, none of the predictor variables had VIF scores exceeding 10, suggesting no significant multicollinearity concerns. However, when applying the FR method, four specific variables (SPI, Aspect, Plan curvature, and Distance to river) had VIF values above the threshold of 10. Consequently, these variables were removed from the FR analysis to reduce multicollinearity and improve the model's accuracy.

4.3 Landslide susceptibility modeling in Zixing City

We conducted landslide susceptibility prediction in Zixing City using SVM and LightGBM models with three distinct input data methods: IV, CF, and FR. Susceptibility levels were categorized into five classes using the natural breaks classification method. Non-landslide samples were strategically selected by excluding five buffer zones (0.1 km, 0.5 km, etc.) surrounding documented landslide locations.

Overall, the SVM model provided more detailed and accurate classification of landslide susceptibility at smaller scales, effectively identifying high-risk areas. In contrast, the LightGBM model produced more uniform results across all scales. As the scale of the buffer zone increased, the susceptibility distribution results from both models using different input methods tended to converge.

4.3.1 IV-based modeling performance

The IV-derived susceptibility maps (Fig. 4) revealed distinct spatial patterns between the two models across varying buffer distances. At smaller scales, the SVM model demonstrated more detailed classification, with a higher degree of overlap between high susceptibility areas and actual landslide locations. The LightGBM model's classification was smoother, with a lower degree of overlap between high susceptibility areas and actual landslide locations. Notably, this performance discrepancy diminished progressively with increasing buffer distances.

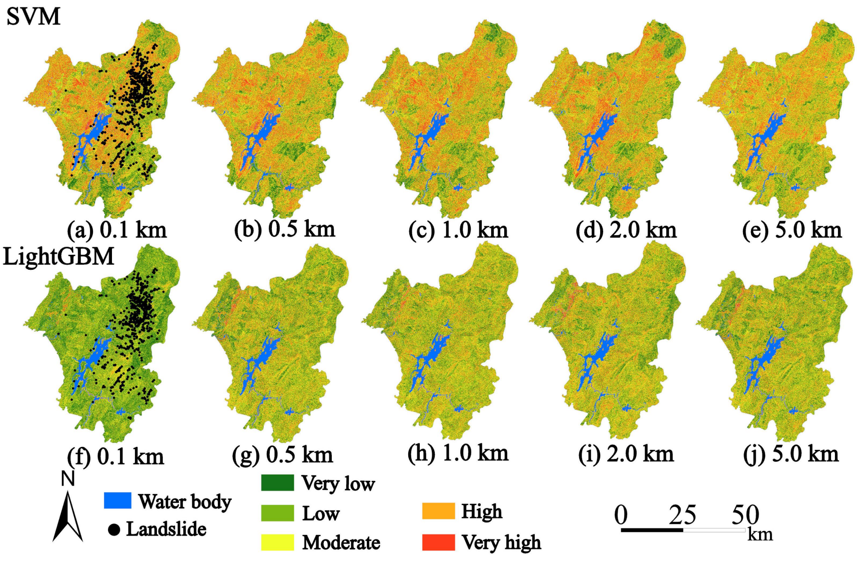

Figure 4. Landslide susceptibility map based on SVM and LightGBM models using the IV input.

4.3.2 CF-based modeling performance

In CF-based modeling (Fig. 5), the SVM model's high and very high landslide susceptibility areas at smaller scales were more extensive than in the IV mode, with actual landslide locations more frequently distributed within these high-risk areas. As the scale increased, the high susceptibility areas gradually decreased. The LightGBM model also showed a relatively smooth distribution, with some high susceptibility areas identified at smaller scales gradually integrating as the scale increased, following a similar trend to the SVM model.

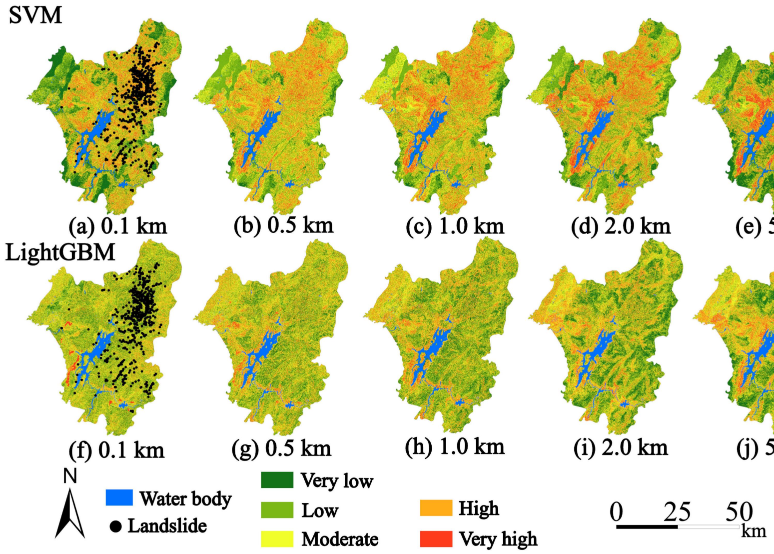

Figure 5. Landslide susceptibility map based on SVM and LightGBM models using the CF input.

4.3.3 FR-based modeling performance

Regarding the FR input (Fig. 6), the SVM model identified a significant number of high and very high landslide susceptibility areas at smaller scales compared to the IV and CF inputs, which closely matched the actual locations of landslides. As the buffer scale expanded, these high-risk areas generally diminished and the distribution became smoother. Conversely, the LightGBM model delivered more uniform results, offering broader moderate-risk distributions, with a small number of high susceptibility areas that did not align with the actual landslide locations. As the scale increased, the high susceptibility areas identified by the LightGBM model gradually diminished, showing greater consistency with the SVM model results at the higher scale.

https://doi.org/10.5194/egusphere-2025-2298
Preprint. Discussion started: 11 August 2025

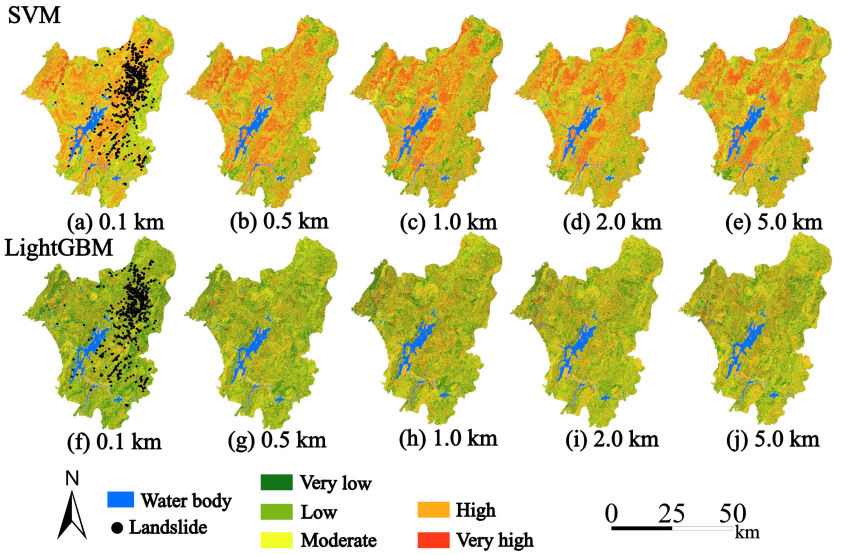

Figure 6. Landslide susceptibility map based on SVM and LightGBM models using the FR input.

4.4 Uncertainty analysis of LSP results

4.4.1 LSP accuracy evaluation and comparative performance

Table 3 presents the training and testing AUC values of SVM and LightGBM models across buffer distances (0.1–5.0 km) and input methods (IV, CF, FR). Both models demonstrated robust predictive performance, with LightGBM consistently outperforming SVM, particularly under FR input conditions.

Table 3. AUC values of different buffer distances under all combined conditions.

Buffer distance (km)	SVM			LightGBM		
	IV	CF	FR	IV	CF	FR
0.1	0.831 (0.769)	0.812 (0.741)	0.720 (0.666)	0.919 (0.832)	0.919 (0.822)	0.915 (0.826)
0.5	0.825 (0.744)	0.820 (0.738)	**0.914 (0.913)**	0.920 (0.811)	0.920 (0.820)	**0.921 (0.920)**
1.0	0.826 (0.744)	0.819 (0.745)	0.721 (0.641)	0.920 (0.809)	0.920 (0.823)	0.916 (0.795)
2.0	0.826 (0.743)	0.834 (0.758)	**0.913 (0.912)**	0.920 (0.805)	0.920 (0.824)	**0.918 (0.918)**
5.0	0.823 (0.731)	0.883 (0.761)	0.721 (0.633)	0.919 (0.803)	0.918 (0.830)	0.916 (0.775)

For SVM, training AUC ranged from 0.720 to 0.914, while testing AUC spanned 0.633 to 0.913. The model showed notable sensitivity to buffer distances with FR input, peaking at 0.913 (0.5 km buffer) but declining to 0.633 at 5.0 km. IV and CF inputs delivered more stable performance (IV: 0.731–0.769; CF: 0.738–0.761), showing minimal overfitting across spatial scales.

LightGBM demonstrated superior consistency, maintaining training AUC >0.915 and testing AUC between 0.775 and 0.920. Its performance peaked at 0.920 with FR input at 0.5 km and 2.0 km buffers, highlighting robustness to spatial variations. Unlike SVM, LightGBM retained high testing AUC (>0.820) for IV and CF inputs across all buffer distances, with only marginal declines for FR at 5.0 km (0.775).

Comparative analysis identified 0.5 km and 2.0 km buffer distances with FR input as optimal configurations. At these distances, both models achieved near-identical training and testing AUC values (SVM: 0.914/0.913 at 0.5 km, 0.913/0.912 at 2.0 km; LightGBM: 0.921/0.920 at 0.5 km, 0.918/0.918 at 2.0 km).

Despite LightGBM’s overall stability, SVM demonstrated distinct advantages at these buffer distances with FR input. While SVM produced less uniform distributions, it captured finer spatial variations in landslide risk, as reflected in its higher mean susceptibility values and better AUC performance. This irregularity in SVM predictions likely indicates greater sensitivity to localized risk patterns at these spatial resolutions.

4.4.2 LSP distribution characteristics across conditions

In addition to the performance metrics, the distribution characteristics of landslide susceptibility predictions revealed fundamental differences between the models (Supplement Figs. S1–S3). LightGBM generated smoother, more symmetrical distributions with lower mean susceptibility values (0.196–0.320) and smaller standard deviations (0.099–0.187), indicating stable and uniform predictions. In contrast, SVM exhibited greater variability, with irregular distributions, higher mean values (0.303–0.515), and larger standard deviations (0.112–0.214). Notably, SVM's mean susceptibility under FR input rose sharply (0.446–

0.515), while LightGBM maintained lower means despite moderately broader deviations (0.160–0.187).

Therefore, SVM is preferable for FR-based modeling at 0.5 km and 2.0 km buffers, where spatial precision is prioritized over prediction uniformity. The SVM model achieved its highest accuracy at the 0.5 km buffer, classifying 86.4% of recorded landslides in high and very high susceptibility zones (Fig. 6 (b)). At the 2.0 km buffer (Fig. 6 (d)), it still correctly classified 82.1% of landslides in these zones. As a result, Fig. 6 (b) is selected as the final landslide susceptibility map.

5 Landslide risk assessment in Zixing City

5.1 Critical rainfall thresholds for landslides in Zixing City

The July 2024 typhoon Gaemi-induced extreme rainfall (412.7 mm average, peaking at 673.9 mm/24h and 132.2 mm/h) triggered a heavy landslide event in Zixing City, Hunan. This event, characterized by granite-weathered soils and slope-side settlements, highlighted critical thresholds for typhoon-induced failures.

Four rainfall threshold models (H1-D7, H12-D7, H24-D7, and H72-D7) were systematically evaluated through 5-fold cross-validation, with their optimal ratio coefficient (RC) thresholds and prediction accuracies summarized in Table 4. The H24-D7 model, which couples 24-hour landfall rainfall with 7-day antecedent moisture—key components of typhoon hydrology—achieved the highest accuracy (71.8%), effectively capturing both cumulative saturation and abrupt triggering by typhoon rainfall bursts. Notably, the H24-D7 model exhibited stable performance across all folds, with accuracy ranging narrowly between 68.8% (Fold 1) and 74.6% (Fold 4), reflecting robust generalizability.

Table 4. Optimal RC values and prediction accuracies (%) for each model across 5-fold cross validation.

Model	Fold 1 RC/Accuracy	Fold 2 RC/Accuracy	Fold 3 RC/Accuracy	Fold 4 RC/Accuracy	Fold 5 RC/Accuracy	Average RC/Accuracy
H1-D7	0.032/56.5	0.062/29.7	0.076/35.5	0.022/53.6	0.040/47.8	0.047/44.6
H12-D7	0.077/54.2	0.167/46.6	0.243/48.3	0.267/47.7	0.154/45.3	0.182/48.5

https://doi.org/10.5194/egusphere-2025-2298
Preprint. Discussion started: 11 August 2025

H24-D7	0.472/68.8	0.436/72.3	0.422/73.1	0.459/74.6	0.414/70.2	**0.440/71.8**
H72-D7	0.789/56.5	0.776/59.4	0.781/63.1	0.802/51.4	0.783/60.1	0.787/58.1

In contrast, the H1-D7 and H12-D7 models displayed marked instability: H1-D7 accuracy fluctuated between 29.7% (Fold 2) and 56.5% (Fold 1), while H12-D7 thresholds (RC12: 0.077–0.267) corresponded to accuracies of 45.3–48.3%. The H72-D7 model showed moderate performance variability (accuracy: 51.4–63.1%) despite consistently high RC72 thresholds (>0.78).

These results highlight the critical role of temporal rainfall parameter selection. The superior performance of the H24-D7 model—combining 24-hour short-term rainfall (H24) and 7-day antecedent rainfall (D7)—suggests that a 24-hour duration optimally captures both immediate landslide triggers and cumulative hydrological effects, balancing sensitivity and stability. This contrasts with shorter (H1/H12) or longer (H72) durations, which either overemphasize transient rainfall spikes or dilute critical triggering signals.

5.2 Spatio-temporal distribution of rainfall thresholds

Fig. 7 illustrates the spatial distribution of rainfall-triggered landslide thresholds derived from four models (RC1, RC12, RC24, and RC72) across multiple temporal scales (1-hour, 12-hour, 24-hour, 72-hour, and 7-day) within the study area.

5.2.1 Short-term predictions (1-hour to 12-hour scales)

At the 1-hour scale (Fig. 7 (a)), the RC1 model generated thresholds ranging from 7 to 50 mm, with 65.2% of landslides occurring in moderate threshold zones (20-30 mm). This indicates the model's effectiveness in detecting slope failures under short-duration rainfall. In contrast, the RC12 model on the 12-hour scale (Fig. 7 (b)) showed a wider threshold range (25-200 mm), with 62.9% of landslides in mid-to-high threshold regions (80-130 mm). This mismatch suggests that the 12-hour cumulative data may underestimate rainfall impacts in specific topographic settings.

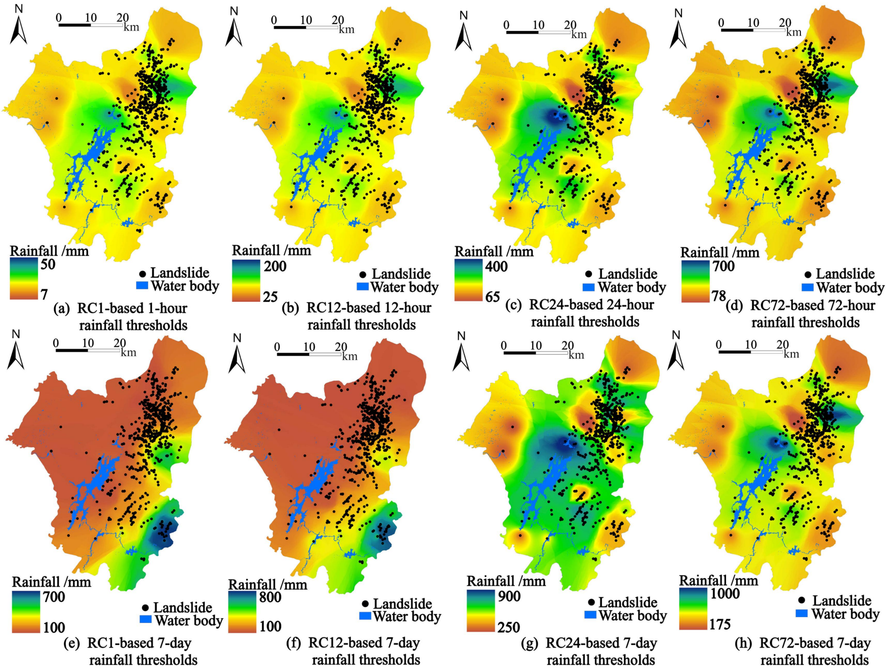

(a) RC1-based 1-hour rainfall thresholds
(b) RC12-based 12-hour rainfall thresholds
(c) RC24-based 24-hour rainfall thresholds
(d) RC72-based 72-hour rainfall thresholds
(e) RC1-based 7-day rainfall thresholds
(f) RC12-based 7-day rainfall thresholds
(g) RC24-based 7-day rainfall thresholds
(h) RC72-based 7-day rainfall thresholds

Figure 7. Distribution of typhoon rainfall thresholds under the optimal RC ratio in Zixing City.

5.2.2 Mid-term predictions (24-hour to 72-hour scales)

The RC24 model at the 24-hour scale (Fig. 7 (c)) displayed a threshold range of 65-400 mm, with 87.1% of landslides occurring within moderate thresholds (100-250 mm) and 12.3% in higher thresholds (>250 mm). This indicates a more accurate capture of rainfall intensity effects. At the 72-hour scale (Fig. 7 (d)), the RC72 model produced thresholds between 78-700 mm, with 59.2% of landslides in mid-to-high threshold regions (200-500 mm). Although the RC72 model demonstrated reasonable sensitivity to prolonged rainfall, its upper threshold (700 mm) may result in conservative risk predictions for some geological settings.

5.2.3 Long-term predictions (7-day scale)

At the 7-day scale, significant differences emerge across models in terms of predicted rainfall thresholds and landslide points. The RC1 model (Fig. 7 (e)) shows a threshold range of 100-700 mm, with landslide points predominantly concentrated in the lower rainfall ranges.

While these low-threshold landslides may indicate localized risks, the model's conservative threshold distribution fails to effectively capture landslides triggered by higher rainfall amounts, potentially overlooking more significant events.

The RC12 model (Fig. 7 (f)), with a threshold range of 100-800 mm, also shows a concentration of landslide points in the lower rainfall ranges. Despite a wider threshold range, the similarity to the RC1 model suggests that RC12 may also underutilize its capacity to predict higher typhoon-induced landslides, leading to under-prediction in areas experiencing moderate to heavy precipitation.

In contrast, the RC24 model (Fig. 7 (g)) exhibits a balanced threshold range (250-900 mm) and effectively identifies landslide points in both moderate and high rainfall categories. This balance enables RC24 to capture the full spectrum of typhoon-induced landslides, accurately identifying risks across different rainfall intensities.

The RC72 model (Fig. 7 (h)) shows a concentration of landslide points in the higher rainfall range (175-1000 mm). While it predicts landslides accurately under heavy rainfall conditions, the model may overestimate risks in some regions and neglect potential landslides associated with lower rainfall thresholds.

Based on the above analysis, the RC24 model is the optimal choice, which aligns with the finding in Section 5.1. Its effectiveness is evident as it demonstrates superior stability and accuracy in both the 24-hour and 7-day timescales. The RC24 model's balanced threshold range enables it to effectively capture landslide risks across varying rainfall intensities, making it the most reliable choice for practical applications in landslide disaster early warning systems.

5.3 Landslide hazard warning system for Zixing City

Based on the optimal LSP results (Fig. 6 (b)) and the validated RC24 rainfall threshold model, a spatially explicit landslide hazard warning system was established for Zixing City.

https://doi.org/10.5194/egusphere-2025-2298
Preprint. Discussion started: 11 August 2025

The integration of spatial probability (LSP) and temporal probability (rainfall thresholds) followed the matrix classification outlined in Table 1.

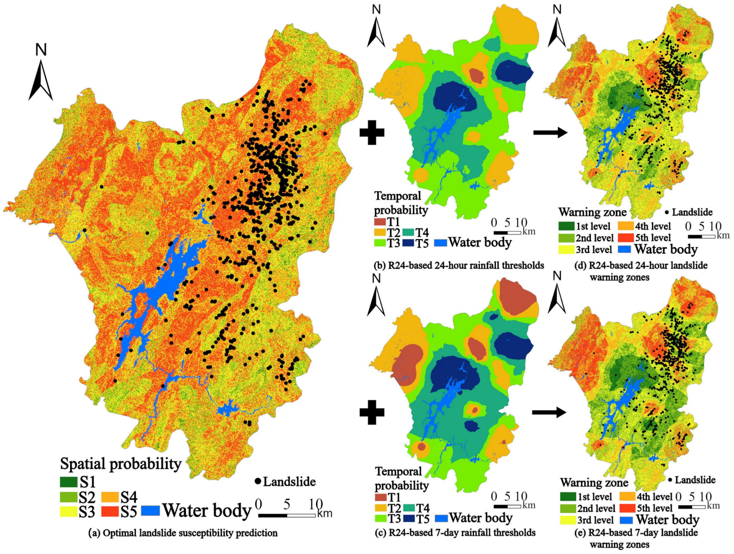

(a) Optimal landslide susceptibility prediction
(b) R24-based 24-hour rainfall thresholds
(c) R24-based 7-day rainfall thresholds
(d) R24-based 24-hour landslide warning zones
(e) R24-based 7-day landslide warning zones

Figure 8. Landslide hazard warning zones in Zixing City.

Five susceptibility levels in the LSP map (Fig. 6 (b)) were replaced with five spatial probabilities (S1–S5) (Fig. 8 (a)), respectively. Simultaneously, the spatially interpolated 24-hour rainfall thresholds (H24) (Fig. 8 (b)) and 7-day effective rainfall thresholds (D7) (Fig. 8 (c)) derived from the RC24 model were classified into five temporal probability levels (T1–T5) using the natural breaks method. Spatial overlay analysis was performed to combine the susceptibility levels (S1–S5) with the rainfall threshold levels (T1–T5), generating two hazard warning zone maps: one based on the 24-hour rainfall thresholds (H24-D7) (Fig. 8 (d)) and the other on the 7-day effective rainfall thresholds (D7-H24) (Fig. 8 (e)).

In the 24-hour threshold system (Fig. 8 (d)), a significant portion of the study area was classified as high to very high warning zones (Levels 3–5), particularly in the central region. These areas are characterized by steep slopes (>21.80°; yellow to dark red regions in Fig. 2 (b)), weathered granite lithology (pink areas in Fig. 2 (l)), proximity to roads (0–800 m; blue zones in Fig. 2 (g)), and moderate-to-distant distances from fracture zones (2,000–7,000 m;

https://doi.org/10.5194/egusphere-2025-2298
Preprint. Discussion started: 11 August 2025

light green regions in Fig. 2 (i)). The high-susceptibility zones (S4–S5), combined with lower rainfall thresholds (T4–T5), indicate acute sensitivity to short-term intense rainfall. Notably, these high-level warning zones overlap with 71.4% of historical landslide occurrences, underscoring the immediate threat posed by short-duration heavy rainfall events.

In contrast, the 7-day threshold system (Fig. 8 (e)) exhibits a similar distribution of high to very high warning zones (Levels 3–5) but with expanded coverage into the northern and eastern parts of the study area. These regions reflect the interaction of prolonged antecedent rainfall (D7) with moderate-to-very-high susceptibility (S3–S5). Topographically, these areas feature greater rainfall accumulation (steep slopes in Fig. 2 (b)) and are predominantly underlain by granite lithology (large pink zones in Fig. 2 (l)). Additionally, they are adjacent to roads (blue and green regions in Fig. 2 (g)) and closer to fracture zones (green and light yellow areas in Fig. 2 (i)). This broader spatial distribution captures sustained risks associated with cumulative rainfall, highlighting zones vulnerable to prolonged precipitation. The alignment of these warning zones with 68.7% of historical landslide sites further validates the effectiveness of the 7-day model in detecting cumulative hydrological effects.

6 Discussion

6.1 Optimization of landslide susceptibility prediction

The comparative analysis of SVM and LightGBM models across different input methods (IV, CF, FR) and buffer distances revealed important insights into the optimization of landslide susceptibility prediction under typhoon rainfall conditions. While LightGBM generally exhibited higher overall accuracy and stability, SVM demonstrated superior performance at specific spatial scales (0.5–2.0 km buffers), capturing localized slope instability patterns induced by typhoon-driven hydrological processes. This finding aligns with previous studies highlighting SVM's effectiveness in modeling non-linear interactions between typhoon rainfall intensity and terrain features (Kalantar, 2018; Zhao et al., 2021).

The optimal performance of SVM at intermediate buffer distances (0.5–2.0 km) suggests a critical balance between typhoon-induced local heterogeneity (e.g., soil saturation variations) and regional geological controls. This range effectively isolates slope units most vulnerable to short-duration typhoon rainfall pulses, while filtering out noise from distant stable areas. The superiority of the FR input method underscores its ability to quantify typhoon-specific factor interactions, such as road density amplifying runoff concentration in granite-weathered slopes (Liu et al., 2022). These results emphasize the necessity of typhoon-adapted spatial scaling in susceptibility modeling, supporting the spatial correlation principles established by Reichenbach et al. (2018).

6.2 Rainfall threshold modeling and spatio-temporal distribution

The evaluation of multiple rainfall threshold models (H1-D7, H12-D7, H24-D7, and H72-D7) revealed that the H24-D7 model was the most effective for predicting typhoon-triggered landslides. This model combines 24-hour typhoon rainfall bursts with 7-day antecedent moisture from tropical cyclones, achieving an accuracy of 71.8%. It strikes a balance between capturing immediate slope failure during typhoon landfall and accounting for prolonged saturation due to pre-typhoon rainfall. In contrast, the shorter (H1/H12) and longer (H72) durations misrepresented the rainfall dynamics specific to typhoons. This finding aligns with Long et al. (2020), who emphasized the importance of integrating both short-term intensity and long-term saturation to predict debris flows.

Spatial thresholds derived from the H24-D7 model demonstrated distinct rainfall gradients related to typhoon exposure. In southeastern slopes, which are more exposed to prevailing typhoon tracks (Fig. 7c), higher thresholds (>250 mm) were observed. This is consistent with Cai et al. (2023), who found that areas directly in the path of typhoons typically experience more intense rainfall due to the influence of the typhoon’s core. These regions are often impacted by the high-intensity convective cores of typhoons. In contrast, northern valleys, influenced by cumulative typhoon rainbands, exhibited lower thresholds (100-150 mm). As Lin et al. (2019) pointed out, typhoon rainbands generate widespread, cumulative rainfall that can be further amplified by topography, such as in valleys where terrain traps moisture and enhances precipitation accumulation. This mechanism explains the lower triggering thresholds in these regions compared to the slopes directly exposed to typhoon tracks.

The spatial gradient observed in the H24-D7 thresholds reflects the dual rainfall modes of typhoons: convective cores with high-intensity bursts and stratiform bands with prolonged drizzle. This highlights the need for typhoon-specific models that can capture both microscale (e.g., storm cell) and macroscale (e.g., rainband) dynamics. Many existing models fail to address these complexities (Segoni et al., 2018b; Guzzetti et al., 2020). The H24-D7 model, by incorporating these spatial gradients and rainfall modes, represents a significant advancement in accurately predicting typhoon-induced landslides.

6.3 Integration of susceptibility and rainfall thresholds for hazard warning

The integration of landslide susceptibility maps with spatially distributed rainfall thresholds resulted in a comprehensive hazard warning system for Zixing City. This approach, combining spatial probability (LSP) and temporal probability (rainfall thresholds), addresses the limitations of traditional, uniform threshold-based warning systems by accounting for local variations in landslide susceptibility. The resulting hazard warning maps based on 24-hour and 7-day rainfall thresholds provide complementary information on short-term and long-term landslide risks.

The high overlap between identified high-risk zones and historical landslide occurrences (71.4% for 24-hour and 68.7% for 7-day thresholds) validates the effectiveness of this integrated approach. These results support the findings of Segoni et al. (2018a) and Piciullo et al. (2018), who emphasized the importance of considering both spatial and temporal factors in landslide hazard assessment. The distinct spatial patterns observed in the 24-hour and 7-day warning maps highlight the different mechanisms of landslide triggering associated with short-duration intense rainfall and prolonged precipitation, respectively.

6.4 Implication for landslide risk management

The developed framework, tailored to the unique challenges posed by typhoon rainfall, has far-reaching implications for enhancing landslide risk management strategies in typhoon-prone regions. By precisely linking the spatial distribution of landslide susceptibility with the dynamic patterns of typhoon - induced rainfall, the hazard warning system provides highly targeted and actionable information. This enables authorities to allocate disaster prevention and mitigation resources more efficiently, focusing efforts on areas most vulnerable to the dual threats of typhoon-related short-term intense rainfall and prolonged antecedent precipitation.

For instance, in Zixing City, the system can identify regions where slopes are already saturated due to pre-typhoon rainfall and are thus highly susceptible to failure during the typhoon’s high-intensity rainfall phase. Such targeted identification allows for the implementation of pre-emptive measures, such as evacuation plans, slope stabilization work, and road closures in these high-risk areas. Moreover, the ability to distinguish between areas at risk from short-term intense rainfall bursts and those vulnerable to the cumulative effects of prolonged typhoon-associated precipitation enables the development of customized response strategies. This not only improves the effectiveness of early warning systems but also enhances overall public safety during typhoon events.

The methodology’s adaptability, which allows for the incorporation of various machine learning algorithms, input methods, and rainfall parameterizations, is particularly valuable in diverse typhoon-affected geological and climatic settings. It can be adjusted to account for the specific characteristics of different typhoon tracks, intensities, and the unique geo-environmental conditions of each region, thereby meeting the urgent need for region - specific landslide hazard assessment tools in the context of typhoon-induced disasters.

6.5 Limitations and future research directions

Despite the significant advancements made in this study, several limitations exist, especially when considering the complex and dynamic nature of typhoon - induced landslides. Firstly, the model validation predominantly depends on a single landslide event triggered by Typhoon “Gemei” in July 2024. Typhoons vary greatly in intensity, rainfall patterns, and tracks, and relying on a single event may not fully capture the diversity of conditions that can lead to landslides during typhoon occurrences. Future research should incorporate multiple landslide events triggered by different typhoons across various seasons and years. This will help to enhance the robustness and generalizability of the results, ensuring that the hazard warning system can perform reliably under a wide range of typhoon-related scenarios.

Secondly, the current study primarily focuses on rainfall - induced landslides triggered by typhoons, overlooking other potential triggering factors that often interact with typhoon rainfall. For example, in some regions, pre-existing seismic activities or ongoing human construction projects in mountainous areas can significantly increase the likelihood of slope failure during typhoons. Future work should explore the integration of multiple triggering mechanisms, such as earthquakes, human-induced slope modifications, and typhoon rainfall, into the hazard assessment framework. This integrated approach will provide a more comprehensive understanding of the complex processes leading to landslides during typhoon events.

Furthermore, the study does not explicitly consider the potential impacts of climate change on typhoon rainfall patterns and landslide occurrence. Climate change is known to alter the frequency, intensity, and track of typhoons, which in turn can have profound effects on landslide risks. Given the increasing frequency and intensity of extreme precipitation events associated with typhoons due to climate change, future studies should incorporate climate projections specific to typhoon-prone regions. This will enable the development of more forward - looking hazard warning systems that can anticipate and adapt to the changing nature of typhoon-induced landslide threats.

Finally, although this study demonstrates the effectiveness of machine learning approaches in landslide susceptibility modeling under typhoon conditions, there is ample room for improvement. Further research should explore advanced deep learning techniques and ensemble methods that can better handle the complex and nonlinear relationships between typhoon-related variables (such as rainfall intensity, duration, and antecedent moisture) and slope stability. These advanced methods may offer improved predictive capabilities, more accurate uncertainty quantification, and ultimately, more reliable hazard warnings for typhoon-induced landslides.

7 Conclusions

This study presents an integrated framework for optimizing landslide susceptibility prediction and rainfall threshold modeling to develop a comprehensive hazard warning system for Zixing City, China. The key conclusions are as follows:

(1) The comparative analysis of SVM and LightGBM models revealed that SVM with FR input at 0.5 km and 2.0 km buffer distances achieved optimal performance in landslide susceptibility prediction. This highlights the importance of careful consideration of spatial scale and input variable selection in susceptibility modeling.

(2) The H24-D7 model, integrating 24-hour typhoon rainfall bursts and 7-day antecedent moisture—key components of typhoon hydrology—achieved the highest accuracy (71.8%), revealing how typhoon-induced saturation and intense rainfall synergistically drive slope failure.

(3) The typhoon-adapted hazard warning system, merging susceptibility maps with dynamic rainfall thresholds, showed 71.4% overlap with historical landslides, confirming the utility of linking spatial slope vulnerability to typhoon rainfall patterns.

(4) The 24-hour and 7-day warning maps unveiled divergent failure mechanisms: short-term typhoon downpours triggering abrupt slope failures vs. prolonged antecedent rainfall inducing gradual soil saturation, underscoring the need for temporally explicit hazard assessments.

(5) The developed framework demonstrates significant potential for improving landslide risk management by providing spatially explicit hazard warnings that account for both inherent susceptibility and dynamic rainfall conditions.

Code and data availability. The source code and data will be made available on request.

Competing interests. The contact author has declared that none of the authors has any competing interests.

Author contributions. **Weifeng Xiao**: Writing-review & editing, Validation, Conceptualization. **Guangchong Yao**: Visualization, Validation, Data curation. **Zhenghui Xiao**: Writing-review & editing, Formal analysis. **Luguang Luo**: Visualization, Validation, Investigation, Data curation. **Yunjiang Cao**: Visualization, Formal analysis, Data curation. **Wei Yin**: Validation, Investigation, Correspondence.

Acknowledgments. This research was funded by the Research Project on Natural Resources of Hunan Provincial Department of Natural Resources (No. HBZ20240112), the Open Research Topic of Hunan Geological Disaster Monitoring Early Warning and Emergency Rescue

Engineering Technology Research Center (No. hndzgczx202409), and the Hunan Provincial Natural Science Foundation of China (No. 2023JJ30238).

References

Achu, A. L., Aju, C. D., Pham, Q. B., Reghunath, R., and Anh, D. T.: Landslide susceptibility modeling using hybrid bivariate statistical - based machine - learning method in a highland segment of Southern Western Ghats, India, Environ. Earth Sci., 81, 361, https://doi.org/10.1007/s12665-022-10464-z, 2022.

Caine, N.: The rainfall intensity: duration control of shallow landslides and debris flows, Geog. Ann. A., 62, 23–27, https://doi.org/10.2307/520449, 1980.

Chang, Z. L., Huang, J. S., Huang, F. M., Bhuyan, K., Meena, S. R., and Catani, F.: Uncertainty analysis of non - landslide sample selection in landslide susceptibility prediction using slope unit - based machine learning models, Gondwana Res., 117, 307–320, https://doi.org/10.1016/j.gr.2023.02.007, 2023.

Chen, W., Pourghasemi, H. R., and Zhao, Z.: A GIS - based comparative study of Dempster - Shafer, logistic regression and artificial neural network models for landslide susceptibility mapping, Geocarto Int., 32, 367–385, https://doi.org/10.1080/10106049.2016.1140824, 2017.

Chen, W., Xie, X. S., Wang, J. L., Pradhan, B., Hong, H. Y., Bui, D. T., Duan, Z., and Ma, J. Q.: A comparative study of logistic model tree, random forest, and classification and regression tree models for spatial prediction of landslide susceptibility, Catena, 151, 147–160, https://doi.org/10.1016/j.catena.2016.11.032, 2017.

Ciurleo, M., Cascini, L., and Calvello, M.: A comparison of statistical and deterministic methods for shallow landslide susceptibility zoning in clayey soils, Eng. Geol., 223, 71–81, https://doi.org/10.1016/j.enggeo.2017.04.023, 2017.

Dou, H. Q., He, J. B., Huang, S. Y., Jian, W. B., and Guo, C. X.: Influences of non - landslide sample selection strategies on landslide susceptibility mapping by machine learning, Geomat. Nat. Haz. Risk, 14, 1–15, https://doi.org/10.1080/19475705.2023.2285719, 2023.

Fan, W., Wei, X. S., Cao, Y. B., and Zheng, B.: Landslide susceptibility assessment using the certainty factor and analytic hierarchy process, J. Mt. Sci., 14, 906–925, https://doi.org/10.1007/s11629-016-4068-2, 2017.

Fan, W., Wei, Y. N., and Deng, L. S.: Failure modes and mechanisms of shallow debris landslides using an artificial rainfall model experiment on Qin-ba Mountain, Int. J. Geomech., 18, 04017157, https://doi.org/10.1061/(ASCE)GM.1943 - 5622.0001068, 2018.

Froude, M. J., and Petley, D. N.: Global fatal landslide occurrence from 2004 to 2016, Nat. Hazards Earth Syst. Sci., 18, 2161–2181, https://doi.org/10.5194/nhess - 18 - 2161 - 2018, 2018.

Gariano, S. L., and Guzzetti, F.: Landslides in a changing climate, Earth - Sci. Rev., 162, 227–252, https://doi.org/10.1016/j.earscirev.2016.08.011, 2016.

Guo, W. X., Ye, J., Liu, C. B., Lv, Y. J., Zeng, Q. Y., and Huang, X.: An approach for predicting landslide susceptibility and evaluating predisposing factors, Int. J. Appl. Earth Obs., 135, 104217, https://doi.org/10.1016/j.jag.2024.104217, 2024.

Guzzetti, F., Gariano, S. L., Peruccacci, S., Brunetti, M. T., Marchesini, I., Rossi, M., and Melillo, M.: Geographical landslide early warning systems, Earth - Sci. Rev., 200, 102973, https://doi.org/10.1016/j.earscirev.2019.102973, 2020.

Guzzetti, F.: Invited perspectives: Landslide populations - can they be predicted?, Nat. Hazards Earth Syst. Sci., 21, 1467–1471, https://doi.org/10.5194/nhess - 21 - 1467 - 2021, 2021.

Huang, F., Cao, Z. S., Guo, J. F., Jiang, S. H., Li, S., and Guo, Z. Z.: Comparisons of heuristic, general statistical and machine learning models for landslide susceptibility prediction and mapping, Catena, 191, 104580, https://doi.org/10.1016/j.catena.2020.104580, 2020.

Huang, F., Cao, Y., Li, W., Catani, F., Song, G., Huang, J., and Yu, C.: Uncertainties of landslide susceptibility prediction: influences of different study area scales and mapping unit scales, Int. J. Coal Sci. Technol., 11, 26, https://doi.org/10.1007/s40789 - 024 - 00678 - w, 2024.

Huang, F., Chen, J., Liu, W., Huang, J., Hong, H., and Chen, W.: Regional rainfall - induced landslide hazard warning based on landslide susceptibility mapping and a critical rainfall threshold, Geomorphology, 408, 108236, https://doi.org/10.1016/j.geomorph.2022.108236, 2022.

Huang, Y., and Zhao, L.: Review on landslide susceptibility mapping using support vector machines, Catena, 165, 520–529, https://doi.org/10.1016/j.catena.2018.03.003, 2018.

Kalantar, B., Pradhan, B., Naghibi, S. A., Motevalli, A., and Mansor, S.: Assessment of the effects of training data selection on the landslide susceptibility mapping: A comparison between support vector machine (SVM), logistic regression (LR), and artificial neural networks (ANN), Geomat. Nat. Haz. Risk, 9, 49–69, https://doi.org/10.1080/19475705.2017.1407368, 2018.

Kenanoglu, M. B., Ahmadi - Adli, M., Toker, N. K., and Huvaj, N.: Effect of unsaturated soil properties on the intensity - duration threshold for rainfall triggered landslides, Tek. Dergi, 30, 9009–9027, https://doi.org/10.18400/tekderg.414884, 2019.

Li, Y. L., Lin, Y. L., and Wang, Y. Q.: A Numerical Study on the Formation and Maintenance of a Long - Lived Rainband in Typhoon Longwang (2005), J. Geophys. Res. Atmos., 124(19), 10401–10426, https://doi.org/10.1029/2019JD030600, 2019.

Liu, L. L., Zhang, Y. L., Xiao, T., and Yang, C.: A frequency ratio - based sampling strategy for landslide susceptibility assessment, Bull. Eng. Geol. Environ., 81, 360, https://doi.org/10.1007/s10064 - 022 - 02836 - 3, 2022.

Lombardo, L., and Mai, P. M.: Presenting logistic regression - based landslide susceptibility results, Eng. Geol., 244, 14–24, https://doi.org/10.1016/j.enggeo.2018.07.019, 2018.

Long, K., Zhang, S. J., Wei, F. Q., Hu, K. H., Zhang, Q., and Luo, Y.: A hydrology - process based method for correlating debris flow density to rainfall parameters and its application on debris flow prediction, J. Hydrol., 589, 125124, https://doi.org/10.1016/j.jhydrol.2020.125124, 2020.

Lv, L., Chen, T., Dou, J., and Plaza, A.: A hybrid ensemble - based deep - learning framework for landslide susceptibility mapping, Int. J. Appl. Earth Obs., 108, 102713, https://doi.org/10.1016/j.jag.2022.102713, 2022.

Marra, F.: Rainfall thresholds for landslide occurrence: systematic underestimation using coarse temporal resolution data, Nat. Hazards, 95, 883–890, https://doi.org/10.1007/s11069-018-3508-4, 2019.

Merghadi, A., Yunus, A. P., Dou, J., Whiteley, J., ThaiPham, B., Bui, D. T., Avtar, R., and Abderrahmane, B.: Machine learning methods for landslide susceptibility studies: A comparative overview of algorithm performance, Earth-Sci. Rev., 207, 103225, https://doi.org/10.1016/j.earscirev.2020.103225, 2020.

Mirus, B. B., Becker, R. E., Baum, R. L., and Smith, J. B.: Integrating real - time subsurface hydrologic monitoring with empirical rainfall thresholds to improve landslide early warning, Landslides, 15, 1909–1919, https://doi.org/10.1007/s10346-018-0995-z, 2018.

Mondini, A. C., Guzzetti, F., and Melillo, M.: Deep learning forecast of rainfall - induced shallow landslides, Nat. Commun., 14, 10.1038/s41467-023-38135-y, https://doi.org/10.1038/s41467-023-38135-y, 2023.

Niu, H. T., Shao, S. J., Gao, J. Q., and Jing, H.: Research on GIS-based information value model for landslide geological hazards prediction in soil - rock contact zone in southern Shaanxi, Phys. Chem. Earth, 133, 103515, https://doi.org/10.1016/j.pce.2023.103515, 2024.

Panchal, S., and Shrivastava, A. K.: A comparative study of frequency ratio, Shannon's entropy and analytic hierarchy process (AHP) models for landslide susceptibility assessment, ISPRS Int. J. Geo-Inf., 10, 603, https://doi.org/10.3390/ijgi10090603, 2021.

Piciullo, L., Calvello, M., and Cepeda, J. M.: Territorial early warning systems for rainfall - induced landslides, Earth-Sci. Rev., 179, 228–247, https://doi.org/10.1016/j.earscirev.2018.02.013, 2018.

Piciullo, L., Gariano, S. L., Melillo, M., Brunetti, M. T., Peruccacci, S., Guzzetti, F., and Calvello, M.: Definition and performance of a threshold - based regional early warning model for rainfall - induced landslides, Landslides, 14, 995–1008, https://doi.org/10.1007/s10346-016-0750-2, 2017.

Pourghasemi, H. R., and Rahmati, O.: Prediction of the landslide susceptibility: Which algorithm, which precision?, Catena, 162, 177–192, https://doi.org/10.1016/j.catena.2017.11.022, 2018.

Regmi, N. R., Walter, J. I., Jiang, J. L., Orban, A. M., and Hayman, N. W.: Spatial patterns of landslides in a modest topography of the Ozark and Ouachita Mountains, USA, Catena, 245, 108344, https://doi.org/10.1016/j.catena.2024.108344, 2024.

Reichenbach, P., Rossi, M., Malamud, B. D., Mihir, M., and Guzzetti, F.: A review of statistically - based landslide susceptibility models, Earth-Sci. Rev., 180, 60–91, https://doi.org/10.1016/j.earscirev.2018.03.001, 2018.

Sahin, E. K.: Comparative analysis of gradient boosting algorithms for landslide susceptibility mapping, Geocarto Int., 37, 2441–2465, https://doi.org/10.1080/10106049.2020.1831623, 2022.

San, B. T.: An evaluation of SVM using polygon-based random sampling in landslide susceptibility mapping: The Candir catchment area (western Antalya, Turkey), Int. J. Appl. Earth Obs., 26, 399–412, https://doi.org/10.1016/j.jag.2013.09.010, 2014.

Segoni, S., Lagomarsino, D., Fanti, R., Moretti, S., and Casagli, N.: Integration of rainfall thresholds and susceptibility maps in the Emilia Romagna (Italy) regional - scale landslide warning system, Landslides, 12, 773–785, https://doi.org/10.1007/s10346-014-0502-0, 2015.

Segoni, S., Piciullo, L., and Gariano, S. L.: A review of the recent literature on rainfall thresholds for landslide occurrence, Landslides, 15, 1483–1501, https://doi.org/10.1007/s10346-018-0966-4, 2018.

Segoni, S., Rosi, A., Lagomarsino, D., Fanti, R., and Casagli, N.: Brief communication: Using averaged soil moisture estimates to improve the performances of a regional - scale landslide early warning system, Nat. Hazards Earth Syst. Sci., 18, 807–812, https://doi.org/10.5194/nhess-18-807-2018, 2018.

Sharma, L. P., Patel, N., Ghose, M. K., and Debnath, P.: Development and application of Shannon's entropy integrated information value model for landslide susceptibility assessment and zonation in Sikkim Himalayas in India, Nat. Hazards, 75, 1555–1576, https://doi.org/10.1007/s11069-014-1378-y, 2015.

Steger, S., Brenning, A., Bell, R., and Glade, T.: The propagation of inventory - based positional errors into statistical landslide susceptibility models, Nat. Hazards Earth Syst. Sci., 16, 2729–2745, https://doi.org/10.5194/nhess-16-2729-2016, 2016.

Sun, D. L., Wu, X. Q., Wen, H. J., and Gu, Q. Y.: A LightGBM-based landslide susceptibility model considering the uncertainty of non-landslide samples, Geomat. Nat. Haz. Risk, 14, 2213807, https://doi.org/10.1080/19475705.2023.2213807, 2023.

Thiene, M., Shaw, W. D., and Scarpa, R.: Perceived risks of mountain landslides in Italy: Stated choices for subjective risk reductions, Landslides, 14, 1077–1089, https://doi.org/10.1007/s10346-016-0741-3, 2017.

Tufano, R., Formetta, G., Calcaterra, D., and De Vita, P.: Hydrological control of soil thickness spatial variability on the initiation of rainfall-induced shallow landslides using a three - dimensional model, Landslides, 18, 3367–3380, https://doi.org/10.1007/s10346-021-01681 - x, 2021.

Wang, H. J., Zhang, L. M., Yin, K. S., Luo, H. Y., and Li, J. H.: Landslide identification using machine learning, Geosci. Front., 12(1), 351–364, https://doi.org/10.1016/j.gsf.2020.02.012, 2021.

Xiao, W. F., Zhou, Z. Y., Ren, B. Z., and Deng, X. P.: Integrating spatial clustering and multi - source geospatial data for comprehensive geological hazard modeling in Hunan Province, Sci. Rep., 15, 1982, https://doi.org/10.1038/s41598-024-84825 - y, 2025.

Yan, F., Zhang, Q. W., Ye, S., and Ren, B.: A novel hybrid approach for landslide susceptibility mapping integrating analytical hierarchy process and normalized frequency ratio methods with the cloud model, Geomorphology, 327, 170–187, https://doi.org/10.1016/j.geomorph.2018.10.024, 2019.

Yang, C., Liu, L. L., Huang, F. M., Huang, L., and Wang, X. M.: Machine learning - based landslide susceptibility assessment with optimized ratio of landslide to non-landslide samples, Gondwana Res., 123, 198–216, https://doi.org/10.1016/j.gr.2022.05.012, 2023.

Yang, K. H., Uzuoka, R., Thuo, J. N., Lin, G. L., and Nakai, Y.: Coupled hydro-mechanical analysis of two unstable unsaturated slopes subject to rainfall infiltration, Eng. Geol., 216, 13–30, https://doi.org/10.1016/j.enggeo.2016.11.006, 2017.

Zêzere, J. L., Pereira, S., Melo, R., Oliveira, S. C., and Garcia, R. A. C.: Mapping landslide susceptibility using data-driven methods, Sci. Total Environ., 589, 250–267, https://doi.org/10.1016/j.scitotenv.2017.02.188, 2017.

Zhang, W. A., Gu, X., Tang, L. B., Yin, Y. P., Liu, D. S., and Zhang, Y. M.: Application of machine learning, deep learning and optimization algorithms in geoengineering and geoscience: Comprehensive review and future challenge, Gondwana Res., 109, 1–17, https://doi.org/10.1016/j.gr.2022.03.015, 2022.

Zhao, Z., Liu, Z. Y., and Xu, C.: Slope unit-based landslide susceptibility mapping using certainty factor, support vector machine, random forest, CF-SVM and CF-RF models, Front. Earth Sci., 9, 589630, https://doi.org/10.3389/feart.2021.589630, 2021.